Optical Materials: X 31 (2026) 100444

Contents lists available at ScienceDirect

Optical Materials: X

journal homepage: www.journals.elsevier.com/optical-materials-x

Mid-infrared emission properties of Er^{3+},Dy^{3+}-codoped CaF_2 crystals

Ngoc Quynh Hoa Nguyen [a], Elena Dunina [b], Liudmila Fomicheva [c], Alexey Kornienko [b], Pavel Popov [d], Sergei Kuznetsov [e], Abdelmjid Benayad [a], Patrice Camy [a], Alain Braud [a,*], Pavel A. Loiko [a,**]

[a] Centre de Recherche sur les Ions, les Matériaux et la Photonique (CIMAP), UMR 6252 CEA-CNRS-ENSICAEN, Université de Caen, 6 Boulevard Maréchal Juin, Cedex 4, Caen, 14050, France
[b] Vitebsk State Technological University, 72 Moskovskaya Ave., Vitebsk, 210035, Belarus
[c] Belarusian State University of Informatics and Radioelectronics, 6 Brovka St., Minsk, 220027, Belarus
[d] Petrovsky Bryansk State University, 14 Bezhitskaya St., Bryansk, 241023, Russia
[e] Prokhorov General Physics Institute of the Russian Academy of Sciences, 38 Vavilova St., Moscow, 119991, Russia

ARTICLE INFO

Keywords:
Laser materials
Calcium fluoride
Mid-infrared
Optical spectroscopy
Luminescence
Judd-Ofelt theory

ABSTRACT

We present a comprehensive spectroscopic investigation of singly Dy^{3+}-doped and Er^{3+},Dy^{3+}-co-doped calcium fluoride (CaF_2) crystals for mid-infrared laser applications around 3 μm and 4.4 μm. The *f–f* transition probabilities of Dy^{3+} were evaluated using a modified Judd–Ofelt formalism that accounts for configuration interaction effects. The stimulated-emission cross section (σ_{SE}) reaches 0.25 × 10^{-20} cm^2 at 2.93 μm for the $^6H_{13/2} \rightarrow {}^6H_{15/2}$ transition, with an emission bandwidth of ~350 nm. This transition exhibits a pronounced phonon sideband extending up to 3.9 μm. The luminescence lifetime of the $^6H_{13/2}$ level decreases from 2.04 to 0.52 ms as the Dy^{3+} concentration raises from 0.1 to 0.5 at.%. Energy transfer from Er^{3+} to Dy^{3+} in codoped crystals is quantified, demonstrating an efficient pathway for sensitized pumping. For the first time, 4.4 μm emission from Dy^{3+}:CaF_2 is observed at room temperature. The interplay between radiative and non-radiative transition rates is analyzed, highlighting the critical role of phonon-assisted relaxation in mid-IR emission. Finally, the potential of other Dy^{3+}-doped fluorite-type hosts, such as SrF_2 and BaF_2, is evaluated.

1. Introduction

Coherent light sources addressing the 3–4 μm mid-infrared spectral range are of strong interest because their emission coincides with fundamental vibrational absorption bands of many molecules, including hydrocarbons, water, and organic functional groups [1]. This makes them relevant for spectroscopy, remote sensing, and environmental monitoring, where strong molecular signatures enable sensitive detection [2–4]. This wavelength region is also well suited for medical applications, as it overlaps with absorption peaks in biological tissues, allowing precise and minimally invasive incisions. Moreover, 3–4 μm sources are valuable for nonlinear optics and mid-IR frequency conversion, where they serve as pump or seed wavelengths for extending laser technologies deeper into the infrared [5].

Direct generation of 3 μm mid-infrared radiation from rare-earth-ion (RE^{3+}) doped materials is feasible with Er^{3+}, Ho^{3+} and Dy^{3+} ions, out of which crystalline and fiber Er-lasers operating on the $^4I_{11/2} \rightarrow {}^4I_{13/2}$ transition are the most widely exploited ones due to efficient pumping at 0.98 μm enabled by InGaAs diode lasers [6–8]. Dysprosium ions (Dy^{3+}) possessing an electronic configuration of [Xe]$4f^9$ (with $^6H_{15/2}$ being the ground state) has attracted a growing attention for laser action in this spectral range as their ultrabroadband emission originating from the quasi-3-level $^6H_{13/2} \rightarrow {}^6H_{15/2}$ transition extends far beyond 3 μm, *i.e.*, it is well detuned from the structured water vapor absorption in air at 2.8 μm, a property being essential for broadband wavelength tuning and, potentially, achieving femtosecond pulses from mode-locked oscillators. The drawbacks of Dy^{3+} include a significant non-radiative path from the $^6H_{13/2}$ manifold reducing the luminescence quantum yield at room temperature (even in fluoride matrices with reasonably low phonon energies), as well as challenging pumping: to maintain low quantum defect, one needs to address non-conventional pump wavelengths in the near-infrared such as 1.1, 1.3, 1.7 or 2.8 μm [8]. Note that

* Corresponding author.
** Corresponding author.
E-mail address: pavel.loiko@ensicaen.fr (P.A. Loiko).

https://doi.org/10.1016/j.omx.2026.100444
Received 15 February 2026; Received in revised form 19 April 2026; Accepted 6 May 2026
Available online 21 May 2026
2590-1478/© 2026 The Authors. Published by Elsevier B.V. This is an open access article under the CC BY license (http://creativecommons.org/licenses/by/4.0/).

Dy^{3+} also offers other emissions in the mid-IR, Fig. 1, in particular, at 4.4 μm (the $^6H_{11/2} \rightarrow {}^6H_{13/2}$ transition) [9]. However, potential laser operation is challenged by the bottleneck effect: the lifetime of the terminal laser level is much longer than that of the emitting state, in part due to the intrinsically higher probability of multiphonon non-radiative relaxation from the $^6H_{11/2}$ manifold [10].

Continuous-wave laser action around 3 μm (on the $^6H_{13/2} \rightarrow {}^6H_{15/2}$ transition) from Dy^{3+}-doped materials at room temperature has been only reported from fluoride glass (ZrF_4- or InF_3-based) fibers. Due to the adaptability of fiber geometry to non-conventional pumping, multiple excitation wavelengths have been exploited so far. Woodward et al. reported on a Dy:ZBLAN fiber laser with in-band (resonant) pumping at 2.83 μm delivering Watt-level output power at 3.15 μm with a high slope efficiency (73%) approaching the Stokes limit [11]. Pumping at 1.7 μm and 1.1 μm (into the $^6H_{11/2}$ and $^6F_{9/2}+{}^6H_{7/2}$ manifolds, respectively) using a Raman-shifted fiber laser and an Yb-fiber source resulted in lower slope efficiencies of 21% and 18%, respectively, achieving a few hundred of mW output powers [12,13]. Regarding single crystals, Johnson and Guggenheim achieved laser emission at 3.02 μm from Dy:BaY_2F_8 under liquid nitrogen temperature [14].

To overcome these limitations, the Er^{3+},Dy^{3+} codoping scheme was proposed as it can simultaneously unlock access to conventional pumping at 0.98 μm, and broaden the overall gain bandwidth around 3 μm by combining the spectral emission profiles from both active ions. The excitation of Er^{3+} ions into the $^4I_{11/2}$ state is followed by a two-step phonon-assisted energy-transfer (ET) to Dy^{3+} ions, as shown in Fig. 1. Wang et al. reported on an Er,Dy:ZBLAN fiber laser broadly tunable from 2.71 to 3.37 μm [15].

Regarding the second appealing mid-IR laser transition of Dy^{3+} around 4.4 μm, very little information can be found in the literature. Barnes and Allen reported on a room temperature Dy:$LiYF_4$ laser at 4.34 μm operating in the free-running regime [9]. Pulsed laser emission from chalcogenide, *i.e.*, Dy:$CaGa_2S_4$ and Dy:$PbGa_2S_4$ [10,16], and chloride, *i.e.*, Dy:KPb_2Cl_5, crystals has also been achieved. Schlosser et al. demonstrated a 1.7-μm diode-pumped Dy:KPb_2Cl_5 laser delivering 1.1 mJ pulses at ~4.4 μm with 12% slope efficiency [17].

Since mid-IR transitions of RE^{3+} ions are strongly affected by non-radiative multiphonon relaxation, host matrices with low phonon energies are desirable. Fluoride crystals, compared with more technologically challenging systems such as chlorides and chalcogenides, represent an attractive compromise between low phonon energy and high optical quality. In particular, fluorite-type alkaline-earth fluorides MF_2 (M = Ca, Sr, Ba, or their mixture) [18,19] are well-established laser host materials due to their high thermal conductivity, low phonon energies, broad optical transparency, and high RE solubility [20,21] retaining the cubic, fluorite-type structure ($M_{1-x}RE_xF_{2+x}$, sp. gr. $Fm\bar{3}m$) [22]. Moreover, at moderate to high doping levels, RE^{3+} ions tend to form clusters [22], leading to strong inhomogeneous broadening of absorption and emission (gain) spectra [23]. As a result, the spectral properties of rare-earth-doped MF_2 crystals more closely resemble those of fluoride glasses than those of ordered crystals such as $LiYF_4$, while still maintaining relatively high thermal conductivity. The growth of RE^{3+}-doped MF_2 crystals is well developed using the Bridgman–Stockbarger and Czochralski methods; however, precise control of the growth atmosphere is required to suppress oxygen impurities that can degrade luminescent performance.

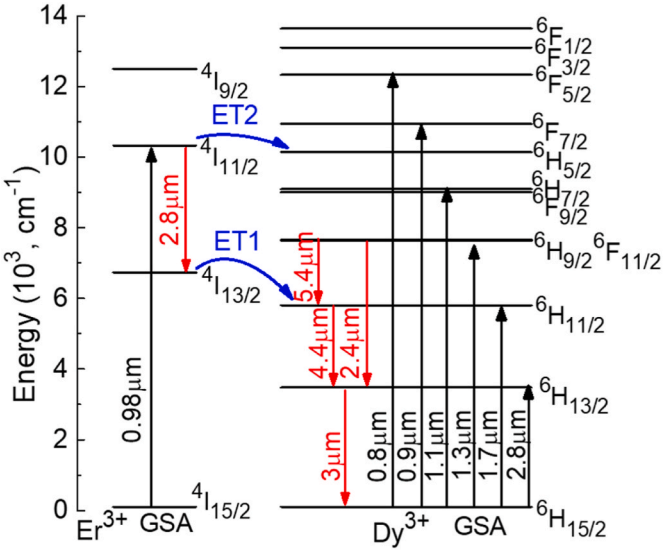

Fig. 1. A partial energy-level scheme of Dy^{3+} and Er^{3+} ions showing pump and laser transitions, GSA – ground-state absorption, ET – phonon-assisted non-radiative energy-transfer.

Er^{3+} and Ho^{3+} doped MF_2-type crystals have been recognized as effective gain media for lasers operating around the 3 μm spectral region [18,24,25]. In contrast, studies on the mid-infrared emission properties of Dy^{3+}-doped fluorite-type crystals – particularly CaF_2 – covering the 3–4.4 μm range remain scarce. Therefore, in the present work, we systematically investigate the spectroscopic properties of Dy^{3+} ions in calcium fluoride crystals for mid-infrared laser applications, focusing on their stimulated-emission properties at 3 μm and 4.4 μm, radiative and non-radiative transition probabilities, and the energy-transfer mechanisms in the Er^{3+}–Dy^{3+} co-doped system.

2. Crystal growth

Single crystals of calcium fluoride (CaF_2), singly doped with Dy^{3+} and codoped with Er^{3+},Dy^{3+} ions, were grown using the Bridgman-Stockbarger technique. The starting powders were high-purity (4 N, *Sigma-Aldrich*) CaF_2 and dysprosium fluoride (DyF_3), the latter of which was obtained by fluorinating dysprosium oxide (Dy_2O_3, 4 N, *Alfa Aesar*) with excess of ammonium hydrogen bifluoride (NH_4HF_2) at 250 °C. For the singly Dy^{3+}-doped crystal, the staring doping level was 0.5 at.% with respect to Ca^{2+} cations ($Ca_{1-x}Dy_xF_{2+x}$) and for the three codoped crystals, the Er concentration was maintained at 3 at.%, while Dy content was 0.1, 0.3 or 0.5 at.%. To avoid the formation of unwanted oxygen-assisted centers and oxyfluoide phases which can degrade the optical quality and spectroscopic properties, the growth chamber was first sealed to vacuum ($<10^{-5}$ mbar) and refilled with a mixture of Ar + CF_4 gases. The precursors were well mixed and placed in the graphite crucible which was then heated at a temperature slightly above the CaF_2 melting point (1418 °C) for 2 h to ensure uniform melting. The crystal growth was enabled by a vertical translation of the graphite crucibles (diameter: Ø8 mm, height: 40 mm) through the hot zone with a temperature gradient of 30 – 40 °C/cm at a rate of 1 – 3 mm/h. Once the growth was completed, the crystals were gradually cooled to room temperature within 72 h. No annealing was applied.

The as-grown crystals had a cylindrical shape (Ø7-8 mm, length: 35 - 40 mm) and they were transparent, without cellular substructure, free of defects and inclusions, Fig. 2. The singly Dy^{3+}-doped crystal was colorless, and the codoped ones had a rose coloration due to Er^{3+} absorption. For spectroscopic studies, we cut cylindrical samples from the central part of the boule having a thickness of 5 mm. The sample was then polished to laser-grade quality on both sides, see Fig. 2(b). The segregation coefficient of Dy^{3+} dopant ions was determined by inductively coupled plasma mass spectrometry (ICP–MS) to be close to unity ($K_{Dy} \approx 1$). The axial distribution of dopant along the cylindrical part of the boule was subsequently assessed by absorption spectroscopy and was found to be uniform, with variations not exceeding 0.05 at.% across 20 mm length in the singly doped crystal.

Crystals adopting the fluorite structure exhibit small enthalpy and entropy changes upon melting. During solidification, their growth is often characterized by the formation of dissipative structures, such as

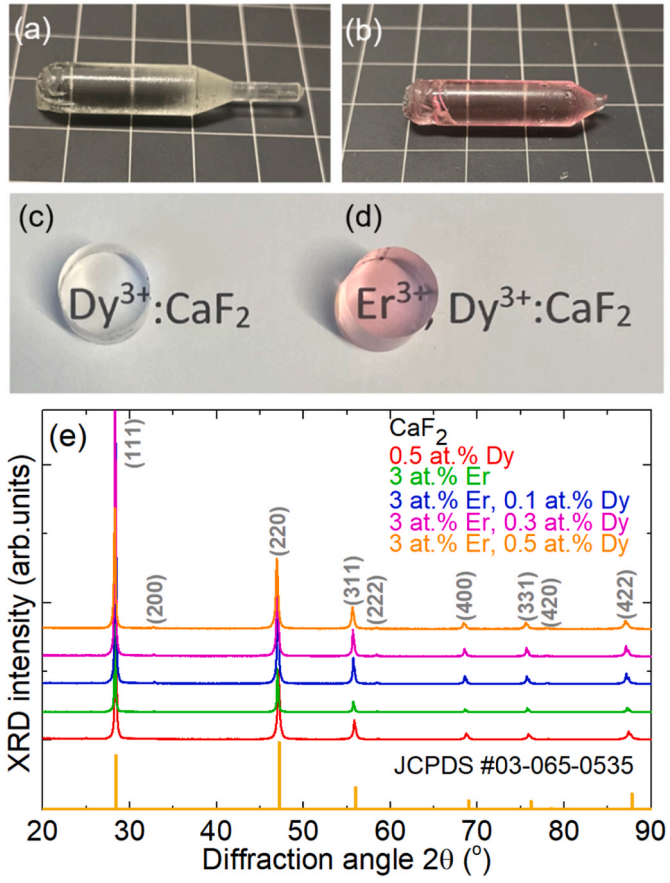

Fig. 2. The photographs of (a,b) as-grown crystal boules and (c,d) laser-grade polished samples of (a,c) singly doped 0.5 at.% Dy^{3+}:CaF_2 and (b,d) codoped 3 at.% Er^{3+}, 0.1 at.% Dy^{3+}:CaF_2. (e) X-ray powder diffraction patterns of the studied crystals, the theoretical pattern for CaF_2 is given (JCPDS card #03-065-0535), (*hkl*) – Miller's indices.

cellular and dendritic morphologies, arising from crystallization of the melt [26]. Optical inhomogeneities are typically attributed to periodic refractive-index variations associated with compositional fluctuations. The instability of the planar solid–liquid interface can be suppressed by employing appropriate growth conditions, specifically a high temperature gradient and a low growth rate, thereby enabling the formation of homogeneous single crystals, as achieved in the present work.

The phase purity (sp. gr. $Fm\bar{3}m$ – O_h^5, No. 225) of the grown crystals has been confirmed using X-ray powder diffraction (XRD) employing a *Rigaku* SmartLab diffractometer (step size: 0.005°, step time: 0.06 s, 2θ range: 20°–95°), Fig. 2(e).

3. Experimental

The thermal conductivity $\kappa(T)$ of a 1 at.% Dy:CaF_2 crystal in the temperature range of 50–300 K was measured by the absolute steady-state longitudinal heat-flow method. The sample had a cylindrical shape with a diameter of 9.6 mm and a length of 37 mm (the analyzed distance corresponds to the 19 mm separation between the thermocouple contact positions). To create a flat (planar) heat front and a uniform distribution of the heat flux along the sample, a resistive heater was attached to one of end faces. The temperature difference along the crystal, induced by the heater, did not exceed 1 K and was monitored using a chromel–(copper + iron) thermocouple. The thermal conductivity coefficient $\kappa(T)$ was calculated using Fourier law, with a measurement error of ±5%. More details can be found elsewhere [27].

The Raman spectra were collected using a confocal Raman microscope (inVia Qontor, *Renishaw*), equipped with a ×50 *Leica* objective and an Ar^+ ion laser (λ_{exc} = 488 nm, 514 nm).

The absorption spectra were measured using a *Varian* CARY 5000 spectrophotometer with a spectral resolution of 0.4 nm to 1.75 nm, depending on the spectral range. The spectra of Dy^{3+} luminescence around 3 μm were measured using an optical spectrum analyzer (OSA, *Yokogawa* AQ6377E) with a spectral resolution of 2 nm. A 1320 nm diode laser served as excitation source. Emission was collected through an uncoated CaF_2 lens and coupled directly into the OSA purged with N_2 gas. The setup was calibrated using a SiC globar lamp (ARCLIGHT-MIR, *Arcoptix*).

The luminescence decay from the $^4I_{13/2}$ and $^4I_{11/2}$ Er^{3+} manifolds was studied using a nanosecond optical parametric oscillator (Horizon, *Continuum*) as excitation source and detected using a set-up consisting of a monochromator (*Oriel* 77200), InGaAs detectors (*Hamamatsu*), a pre-amplifier (DHPCA-100, *FEMTO*) and an 8 GHz digital oscilloscope (DSA70804B, *Tektronix*). The decay from the $^6H_{13/2}$ Dy^{3+} state was measured using 808 nm laser diode as excitation source and detected using a system comprising a monochromator (*Oriel* 74086), a lock-in amplifier (SR810 DSP, *Stanford Research Systems*), and a liquid nitrogen-cooled InSb detector (J10D series, *Judson Infrared*) and the same oscilloscope. The same setup was also employed for measuring the exponential sideband of Dy^{3+} emission between 3.4 and 4 μm.

4. Results and discussions

4.1. Thermal conductivity

The temperature dependence of thermal conductivity of 1 at.% Dy:CaF_2 is illustrated in Fig. 3. Dy^{3+} doping reduces the value of κ as compared to the nominally pure (undoped) crystal, namely from 10.3 $Wm^{-1}K^{-1}$ [28] to 7.0 $Wm^{-1}K^{-1}$ at 300 K, while it remains reasonably high for potential laser applications. One can observe a low-temperature maximum at ~120 K on the $\kappa(T)$ curve. According to the previous studies, for CaF_2 crystals doped with rare-earth ions of the yttrium subgroup (including Dy^{3+}), the dominating type of the formed ion clusters is the large octacubic cluster $(RE_6F_{37})^{19-}$ [29–31]. These structures act as efficient centers of phonon scattering resulting in the observed characteristic shape of the temperature dependence of the thermal conductivity. For comparison, the same figure includes reference data for 3 at.% Er^{3+}:CaF_2, which exhibits a lower thermal conductivity at room temperature (4.3 $Wm^{-1}K^{-1}$), suggesting that codoped crystals are likely to experience pronounced thermal effects.

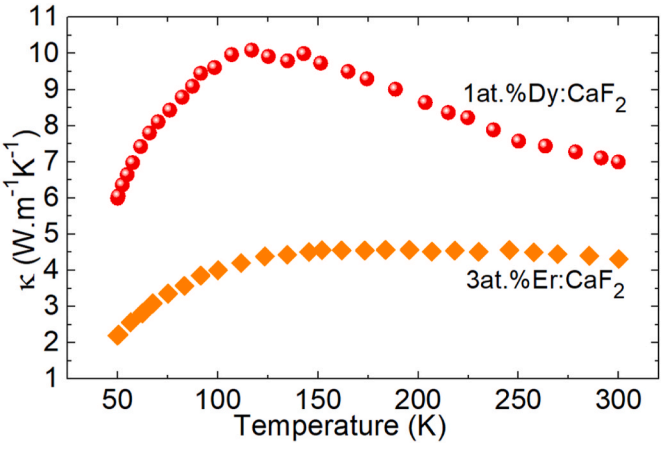

Fig. 3. Temperature dependence of thermal conductivity for 1 at.% Dy^{3+}:CaF_2 and 3 at.% Er^{3+}:CaF_2 crystals.

4.2. Optical absorption

For the singly Dy^{3+}-doped CaF_2 crystal, the absorption bands in the transparency range are related to $4f - 4f$ electronic transitions of Dy^{3+} ion from its ground state, $^6H_{15/2}$. The absorption cross-sections, $\sigma_{abs} = \alpha_{abs}/N_{Dy}$, were calculated from the absorption coefficient α_{abs} and ion density $N_{Dy} = 1.23 \times 10^{20}$ at/cm^3, calculated using the segregation coefficient of Dy^{3+} ions, $K_{Dy} \approx 1$. The σ_{abs} spectra are plotted in Fig. 4(a–f). The electronic transitions of Dy^{3+} ions were assigned according to the energy-level scheme of the free ion reported by Carnall et al. [32]. The absorption bands are broad and almost structureless (they resemble those in Dy^{3+}-doped fluoride glasses, revealing a "glassy-like" behavior) due to the strong inhomogeneous spectral line broadening. The latter originates from the rare-earth ion clustering in CaF_2.

There exist various pumping schemes for mid-infrared Dy^{3+} lasers, addressing the absorption transitions at 0.8 μm ($^6H_{15/2} \rightarrow {}^6H_{5/2}$), 0.9 μm ($^6H_{15/2} \rightarrow {}^6H_{7/2}$), 1.1 μm ($^6H_{15/2} \rightarrow {}^6H_{7/2}+{}^6F_{9/2}$), 1.3 μm ($^6H_{15/2} \rightarrow {}^6H_{9/2}+{}^6F_{11/2}$), 1.7 μm ($^6H_{15/2} \rightarrow {}^6H_{11/2}$), as well as 2.8 μm ($^6H_{15/2} \rightarrow {}^6H_{13/2}$) [11–13,33,34]. When targeting laser emission at 3 μm, resonant (in-band) pumping directly into the upper laser level ($^6H_{13/2}$) is expected to lead to the lowest quantum defect and highest slope efficiency, however, it requires customized pump sources, such as Er-fiber lasers [11]. For the $^6H_{15/2} \rightarrow {}^6H_{13/2}$ Dy^{3+} transition in CaF_2, the peak $\sigma_{abs} = 0.35 \times 10^{-20}$ cm^2 at 2834 nm (absorption bandwidth (FWHM): 144 nm). Progressively reducing the pump wavelength allows one to access more conventional pump sources at the expense of reduced Stokes efficiency and severe thermal effects. For the $^6H_{15/2} \rightarrow {}^6H_{11/2}$ Dy^{3+} transition addressed by Raman-shifted Er-fiber lasers [12], the peak $\sigma_{abs} = 0.16 \times 10^{-20}$ cm^2 at 1692 nm (absorption bandwidth: ~138 nm). Note that this pump scheme will correspond to the resonant excitation of the 4.4-μm laser transition of Dy^{3+} ($^6H_{11/2} \rightarrow {}^6H_{13/2}$).

Dysprosium is a polyvalent ion, and Dy^{2+} can exist in fluorite type crystals similarly to some other divalent-metal rare-earths, notably, Yb^{2+}, Tm^{2+}, Eu^{2+} or Sm^{2+} [35]. Dy^{2+} ions exhibit characteristic absorption in the visible which is not observed in the present work. Dy^{2+}:CaF_2 is one of the earliest laser materials based on both ceramic and single-crystal architectures [36–39].

4.3. Judd-Ofelt theory

The intensities of $4f - 4f$ transitions of Dy^{3+} ions in the 0.5 at.% Dy:CaF_2 crystal were calculated based on the measured absorption spectrum within the modified Judd-Ofelt (mJ-O) theory accounting for weak

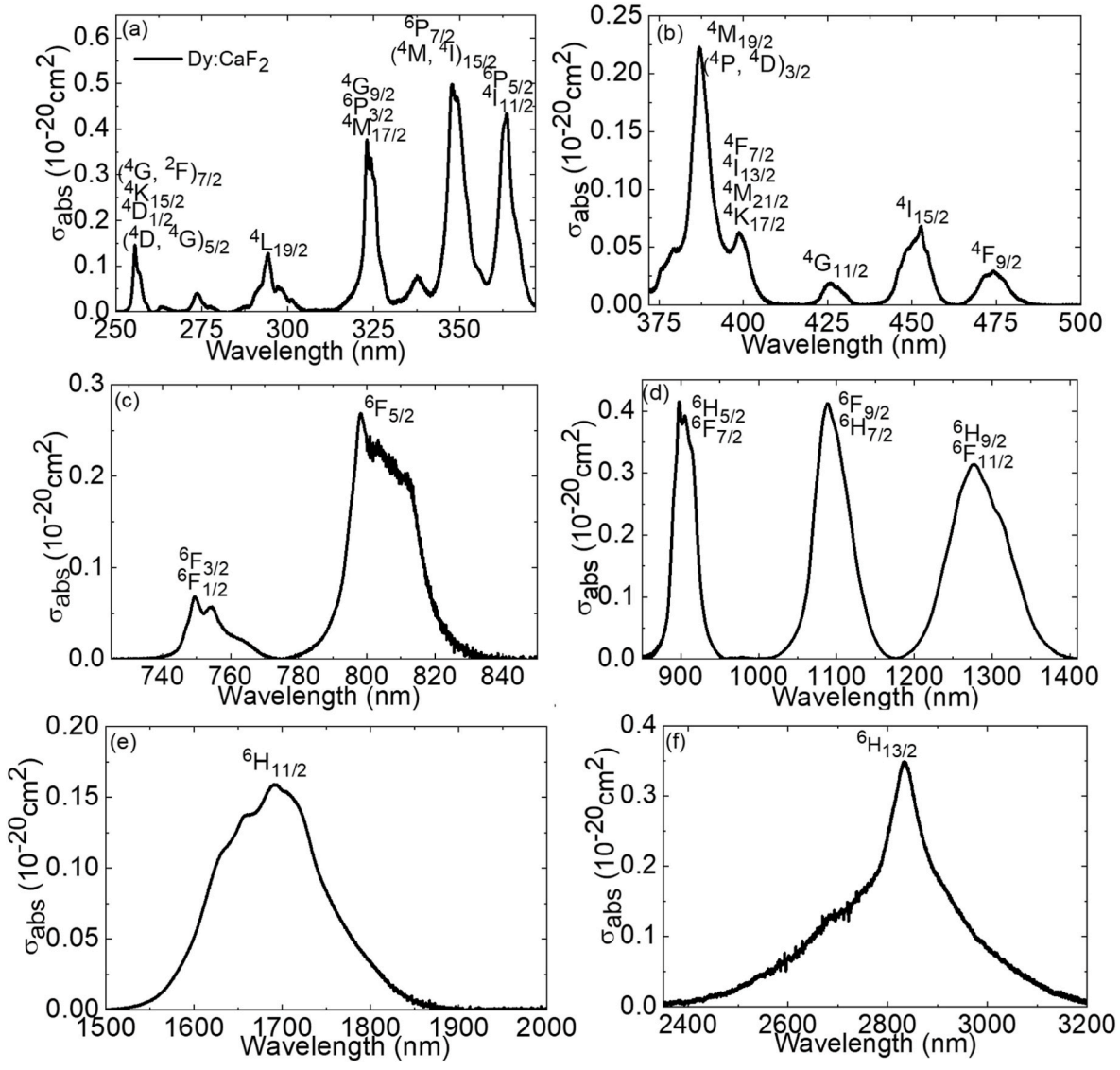

Fig. 4. (a-f) Absorption cross-section (σ_{abs}) spectra of 0.5 at.% Dy^{3+}:CaF_2 crystal.

configuration interaction with the excited configuration of the opposite parity, $4f^{n-1}5d^1$. Within this parametrization scheme, the electric dipole (ED) line strengths of $4f - 4f$ transitions are given by Refs. [40,41]:

$$S_{ff}^{ED}(JJ') = \sum_{k=2,4,6} U^{(k)}\widetilde{\Omega}_k, \tag{1a}$$

$$\widetilde{\Omega}_k = \Omega_k\left[1 + 2\alpha\left(E_J - E_{J'} - 2E_f^0\right)\right], \tag{1b}$$

where $U^{(k)}$ are the reduced squared matrix elements, and the intensity parameters $\widetilde{\Omega}_k$ vary linearly with the energies (E_J and $E_{J'}$) of the two multiplets participating in the optical transition $J \rightarrow J'$, E_f^0 represents the mean energy of the $4f^n$ ground-state configuration and the value of the α parameter is determined by two equivalent mechanisms: covalence effects and excited configurations of opposite parity. Consequently, within the mJ-O theory, there are four free (fitting) parameters, Ω_2, Ω_4, Ω_6, and α.

The experimental, f_{exp}, and calculated, f_{calc}, oscillator strengths for Dy^{3+} transitions observed in absorption are listed in Table 1. The contributions from electric dipole (ED) and magnetic dipole (MD, for $\Delta J = 0, \pm 1$) transitions are included. The latter were calculated separately using the Russell–Saunders approximation on wave functions of Dy^{3+} ions under the assumption of a free-ion. The set of $U^{(k)}$ was calculated using the free-ion parameters reported by Carnall et al. [32] The refractive index of CaF_2 was calculated based on the dispersion relation from Ref. [42]. Γ refers to the absorption coefficient integrated over a band corresponding to a particular transition or a group of undistinguishable (spectrally overlapping) transitions. The use of the mJ-O theory allows to improve the agreement between $<f_{exp}>$ and $<f_{calc}>$, reducing the root mean square (r.m.s.) deviation from 0.521 for the standard J-O theory to 0.280 for the mJ-O one.

The following intensity parameters were obtained: $\Omega_2 = 0.708$, $\Omega_4 = 4.179$, $\Omega_6 = 3.666$ [10^{-20} cm^2] and $\alpha = 0.91 \times 10^{-4}$ cm ($\Delta = 0.55 \times 10^4$ cm^{-1}) for the mJ-O theory and $\Omega_2 = 0.067$, $\Omega_4 = 4.440$, $\Omega_6 = 2.612$ [10^{-20} cm^2] for the standard parametrization scheme. Gao et al. previously investigated Dy^{3+}-doped and Dy^{3+},Y^{3+}-codoped CaF_2 with respect to their visible emission properties. For the Dy^{3+}-doped crystal, they reported the intensity parameters of $\Omega_2 = 0.899$, $\Omega_4 = 0.796$, $\Omega_6 = 2.429$ [10^{-20} cm^2] using the standard J–O analysis [43].

The probabilities of spontaneous radiative transitions of Dy^{3+} ions were calculated using the mJ-O model. The parameters relevant for laser operation in the mid-infrared range are listed in Table 2, namely, the probabilities of spontaneous radiative transitions $A_{calc}^{\Sigma}(JJ')$, the radiative lifetimes τ_{rad} of the $^6H_{13/2}$, $^6H_{11/2}$ and $^6H_{9/2}$ states, and the luminescence branching ratios $\beta_{JJ'}$ for the $^6H_{9/2} \rightarrow {}^6H_{13/2}$, $^6H_{11/2} \rightarrow {}^6H_{13/2}$, and $^6H_{9/2} \rightarrow {}^6H_{11/2}$ transitions giving rise to emission at 2.4 μm, 4 μm and 5.7 μm, respectively.

In particular, the radiative lifetime $\tau_{rad}(^6H_{13/2})$ is 46.67 ms, in good agreement with previous values obtained for a Dy^{3+},Y^{3+}:CaF_2 crystal using standard J-O theory (51.15 ms) [43], as well as with the estimate reported by Fleischman et al. for Dy^{3+}:BaF_2 (45.9 ms), derived from a comparison between the reciprocity method and the Füchtbauer–Ladenburg approach for stimulated-emission cross-section evaluation [44].

Table 1
Intensities[a] of transitions in absorption of dysprosium (III) ions in the 0.5 at.% Dy^{3+}:CaF_2 crystal.

$^6H_{15/2} \rightarrow$	$<E>$,	Γ,	f^{Σ}, 10^{-6}		
	cm^{-1}	cm^{-1}*nm	f_{exp}	f_{calc}^{Σ} (J-O)	f_{calc}^{Σ} (mJ-O)
$^6H_{13/2}$	3537.4	129.720	1.503	$1.430^{ED}+0.330^{MD}$	$1.144^{ED}+0.330^{MD}$
$^6H_{11/2}$	6007.9	34.464	1.117	0.950^{ED}	0.868^{ED}
$^6H_{9/2}+{}^6F_{11/2}$	7750.8	45.557	2.570	3.245^{ED}	2.598^{ED}
$^6F_{9/2}+{}^6H_{7/2}$	9125.9	34.727	2.678	3.534^{ED}	2.874^{ED}
$^6H_{5/2}+{}^6F_{7/2}$	11034	20.312	2.300	2.378^{ED}	2.301^{ED}
$^6F_{5/2}$	12416	8.316	1.189	0.995^{ED}	1.078^{ED}
$^6F_{3/2}+{}^6F_{1/2}$	13239	1.857	0.300	0.189^{ED}	0.209^{ED}
$^4F_{9/2}$	21092	0.488	0.201	0.178^{ED}	0.216^{ED}
$^4I_{15/2}$	22202	0.926	0.421	$0.426^{ED}+0.086^{MD}$	$0.546^{ED}+0.086^{MD}$
$^4G_{11/2}$	23409	0.246	0.125	0.132^{ED}	0.122^{ED}
$^4F_{7/2}+{}^4I_{13/2}+{}^4M_{21/2}+{}^4K_{17/2}$	25798	3.910	2.406	$2.269^{ED}+0.007^{MD}$	$2.830^{ED}+0.007^{MD}$
$^6P_{5/2}+{}^4I_{11/2}+{}^6P_{7/2}+{}^4M_{15/2}+{}^4D_{5/2}+{}^4I_{9/2}$	28637	9.850	7.310	$6.749^{ED}+0.010^{MD}$	$7.216^{ED}+0.010^{MD}$
$^4G_{9/2}+{}^6P_{3/2}+{}^4M_{17/2}$	30771	2.068	1.822	0.911^{ED}	1.408^{ED}
r.m.s deviation				0.521	0.280

[a] $<E>$ – energy of the "center of gravity" of the absorption band, Γ – integrated absorption coefficient; f_{exp} and f_{calc}^{Σ} – experimental and calculated absorption oscillator strengths, respectively, ED and MD – electric-dipole and magnetic-dipole contributions, respectively.

4.4. Stimulated-emission and gain cross-sections at ~3 μm

The stimulated-emission (SE) cross-sections, σ_{SE}, for the $^6H_{13/2} \rightarrow {}^6H_{15/2}$ Dy^{3+} transition at ~3 μm were calculated using the Füchtbauer-Ladenburg (F-L) equation [45]:

$$\sigma_{SE}(\lambda) = \frac{\lambda^5}{8\pi n^2 \tau_{rad} c} \times \frac{\beta(JJ')I(\lambda)}{\int \lambda I(\lambda) d\lambda}, \tag{2}$$

where λ is the wavelength of light, n is the refractive index of the crystal at the mean emission wavelength, c is the speed of light, τ_{rad} is the radiative lifetime of the emitting state ($^6H_{13/2}$), $\beta_{JJ'} = 1$, and $I(\lambda)$ is the measured spectral profile of luminescence for the considered transition calibrated for the apparatus function.

Fig. 5(a) depicts the absorption and SE cross-section spectra of singly Dy^{3+}-doped CaF_2 crystal in the spectral range around 3 μm corresponding to $^6H_{15/2} \leftrightarrow {}^6H_{13/2}$ transition. A significant spectral broadening is also observed for the emission profile, resulting in a broad emission bandwidth (FWHM) of 350 nm. Remarkably, the emission extends far beyond 3 μm avoiding the structured water vapor absorption in the atmosphere. The peak σ_{SE} value reaches 0.25 × 10^{-20} cm^2 at 2947 nm.

3-μm Dy lasers operate on a quasi-3-level scheme due to the inherent reabsorption from the ground-state. Thus, gain cross-sections, $\sigma_{gain} = \sigma_{SE} \times \beta - \sigma_{abs} \times (1 - \beta)$, are calculated to assess the gain bandwidth, the expected laser wavelength and the tuning range, where $\beta = N_2(^6H_{13/2})/N_{Dy}$ is the population inversion ratio. Fig. 5(b) displays the spectral gain profiles for Dy:CaF_2 around 3 μm. On increasing β from 0.2 to 0.45, the maximum in the gain spectra experiences a blue shift from 3284 nm to 3030 nm. At an intermediate β of 0.35, the gain bandwidth (FWHM) is as broad as 338 nm. The broadband gain properties of Dy^{3+}:CaF_2 crystal around 3 μm indicate its potential for generation and amplification of extremely short pulses – down to femtosecond regime and the tunability at these wavelengths.

Table 2
Selected probabilities of spontaneous radiative transitions of Dy^{3+} in CaF_2 crystal.

Transition	$\langle\lambda_{em}\rangle$, nm	$A_{calc}^{\Sigma}(JJ')$, s^{-1}	$\beta_{JJ'}$, %	τ_{rad}, ms
$^6H_{13/2} \rightarrow {}^6H_{15/2}$	2826.9	$15.57^{ED}+6.33^{MD}$	100	45.67
$^6H_{11/2} \rightarrow {}^6H_{13/2}$	4047.8	$3.89^{ED}+3.69^{MD}$	11.9	15.63
$^6H_{9/2} \rightarrow {}^6H_{11/2}$	5737.6	$3.11^{ED}+1.45^{MD}$	1.3	2.81
$\rightarrow {}^6H_{13/2}$	2373.4	$62.39^{ED}+0.68^{MD}$	17.7	

[a] $\langle\lambda_{em}\rangle$ – mean wavelength of the emission band, $\beta_{JJ'}$ – luminescence branching ratio, τ_{rad} – radiative lifetime of the excited state, ED and MD – electric-dipole and magnetic-dipole, respectively.

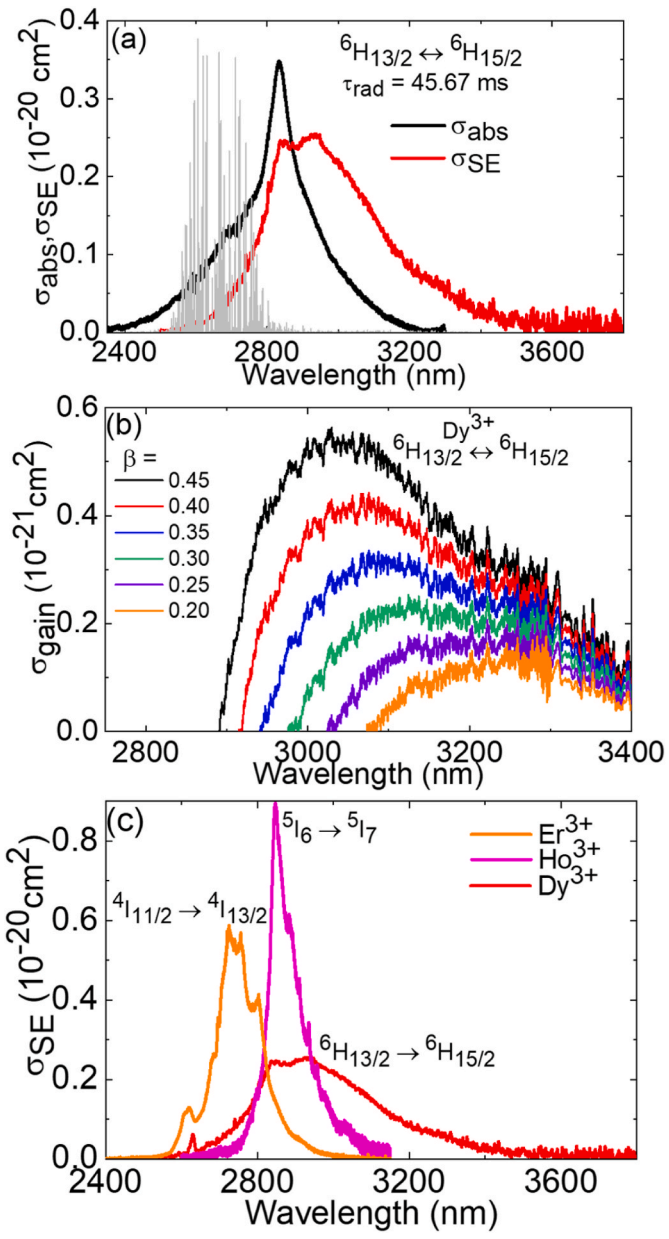

Fig. 5. (a) Absorption, σ_{abs}, and stimulated emission (SE), σ_{SE}, cross-sections for the $^6H_{15/2} \leftrightarrow {}^6H_{13/2}$ transitions of Dy^{3+} ions in CaF_2 crystal, corrected for the structured water vapor absorption in air (in grey, arb. units, according to the HITRAN database); (b) Gain cross-section spectra, $\sigma_{gain} = \sigma_{SE} \times \beta - \sigma_{abs} \times (1 - \beta)$, around 3 μm plotted for different population inversion ratios (β); (c) Comparison of σ_{SE} spectra around 3 μm for Er^{3+}, Ho^{3+} and Dy^{3+} ions in CaF_2.

It is worth comparing the SE cross-section spectra of three rare-earth ions exhibiting luminescence around 3 μm, notably Er^{3+}, Ho^{3+} and Dy^{3+} in CaF_2 crystals, see Fig. 5(c). Among these three ions, Dy^{3+} offers the broadest emission bandwidth covering the range far beyond 3 μm, *i.e.*, being well detuned from the structured water vapor absorption in air, a property being essential for achieving femtosecond pulses from mode-locked oscillators and unlike for Er^{3+} and Ho^{3+}, the $^6H_{13/2} \rightarrow {}^6H_{15/2}$ Dy^{3+} transition is not of self-terminating nature. However, σ_{SE} values for Dy^{3+} ions around 3 μm are about two times lower than those for Er^{3+} and Ho^{3+} ones. This is due to a combination of a relatively long radiative lifetime of the $^6H_{13/2}$ manifold of Dy^{3+}, as well as the large ground-state splitting of this ion, which results in a broadened emission band.

With the goal of acquiring the broader gain bandwidth around 3 μm, it is obvious that a combination of Er^{3+} and Dy^{3+} will be the prospect for the broadly tunable laser potentially covering the wavelength range spanning from 2.7 μm to 3.3 μm as demonstrated earlier for Dy:ZBLAN glass fibers [15].

4.5. Emission properties of Er^{3+},Dy^{3+}-codoped crystals

Codoping of CaF_2 crystals with both Er^{3+} and Dy^{3+} ions serves two aims: i) to combine the spectral gain profiles resulting in broadband emission, and ii) to resolve the main difficulty in exciting mid-infrared Dy^{3+} emission, namely, the relatively weak absorption of this ion and its non-conventional pump wavelengths. The donor (D) Er^{3+} ions can be efficiently pumped at 0.96 μm into the $^4I_{11/2}$ manifold, *e.g.*, by InGaAs diode lasers or Yb-fiber lasers, and there exist two phonon-assisted non-radiative energy-transfer (ET) processes, $^4I_{11/2}(Er^{3+}) \rightarrow {}^6H_{5/2}(Dy^{3+})$ and $^4I_{13/2}(Er^{3+}) \rightarrow {}^6H_{11/2}(Dy^{3+})$, enabling acceptor (A) Dy^{3+} emission around 3 μm and 4.4 μm.

Crystals codoped with 3 at.% Er^{3+} and a various content of Dy^{3+} (ranging from 0.1 to 0.5 at.%) were studied. By exciting the luminescence using an InGaAs laser diode at 960 nm (to the $^4I_{11/2}$ Er^{3+} state), broadband emission around 3 μm originating from both ions was observed. On increasing the Dy content, the emission spectrum progressively broadened extending far beyond 3 μm, and the contribution of this long-wave emission gradually increased, Fig. 6(a). The broadest emission profile was observed for the 3 at.% Er^{3+}, 0.5 at.% Dy^{3+} codoped CaF_2 crystal, exhibiting a bandwidth (FWHM) of 310 nm. By studying the corresponding singly Er^{3+} and Dy^{3+}-doped crystals, the spectrum was deconvoluted and the emission at shorter wavelengths with the most intense peak at 2.8 μm was assigned to Er^{3+} ions ($^4I_{11/2} \rightarrow {}^4I_{13/2}$), while that at longer wavelengths belongs to Dy^{3+} ions ($^6H_{13/2} \rightarrow {}^6H_{15/2}$).

We have also studied the long-wavelength sideband of the $^6H_{13/2} \rightarrow {}^6H_{15/2}$ emission band of Dy^{3+} ions, by sacrificing the spectral resolution to gain higher sensitivity to this weak emission. This emission is due to a phonon-terminated (Stokes) process, and its spans up to at least 3.9 μm, see Fig. 6(c). Note that both Raman (321 cm^{-1}) and IR (466 cm^{-1}) active phonons may participate in this emission. The longest wavelength of a purely electronic transition for Dy^{3+} ions in C_{4v} symmetry sites in CaF_2 is 3.32 μm (3622 cm^{-1} ($^6H_{13/2}$, Δ_7) → 616 cm^{-1} ($^6H_{15/2}$, Δ_7), Δ_i – irreducible representation) [46].

4.6. Luminescence dynamics

First, the luminescence decay from the $^6H_{13/2}$ Dy^{3+} manifold was studied. For the crystal singly doped with 0.5 at.% Dy^{3+}, the mean luminescence lifetime $<\tau_{lum}>$ was measured to be 0.41 ms (the rate of non-radiative relaxation: $W_{NR} = 2.42 \times 10^3$ s^{-1}). Monitoring the luminescence lifetime of the same manifold for the 3 at.% Er^{3+}, x at.% Dy^{3+} codoped CaF_2 crystals, a close value was found for $x = 0.5$ ($<\tau_{lum}> = 0.52$ ms), while a significant increase of the lifetime was observed for crystals with $x = 0.3$ (0.81 ms) and $x = 0.1$ (2.04 ms), see Fig. 7(a). Still, these values are much shorter than the radiative lifetime ($\tau_{rad} = 45.7$ ms) due to the non-negligible multiphonon non-radiative relaxation.

The luminescence lifetimes of the $^4I_{11/2}$ and $^4I_{13/2}$ manifolds of donor Er^{3+} ions in codoped crystals (denoted as $\tau_{D,A}$) were then measured as a function of Dy^{3+} (acceptor) doping level under resonant excitation and compared with those (denoted as τ_D) for a singly 3 at.% Er^{3+}-doped CaF_2 crystal, see Fig. 7(b and c). For the singly-doped crystal, one finds $\tau_D = 3.32$ ms ($^4I_{13/2}$) and 5.72 ms ($^4I_{11/2}$). On increasing the Dy^{3+} doping level x, the $\tau_{D,A}$ lifetimes progressively decrease reaching 0.20 ms ($^4I_{13/2}$) and 0.44 ms ($^4I_{11/2}$) for $x = 0.5$, indicating an efficient energy transfer Er^{3+}(D) → Dy^{3+}(A) promoted by the close proximity of rare-earth ions forming clusters in CaF_2.

The efficiency of $Er^{3+} \rightarrow Dy^{3+}$ energy transfer can be estimated from the measured lifetimes as $\eta_{ET} = 1 - \tau_{D,A}/\tau_D$. For the $^4I_{11/2}(Er^{3+}) \rightarrow {}^6H_{5/2}(Dy^{3+})$ process, η_{ET} increases from 62.4% to 92.3%, and for the $^4I_{13/2}$

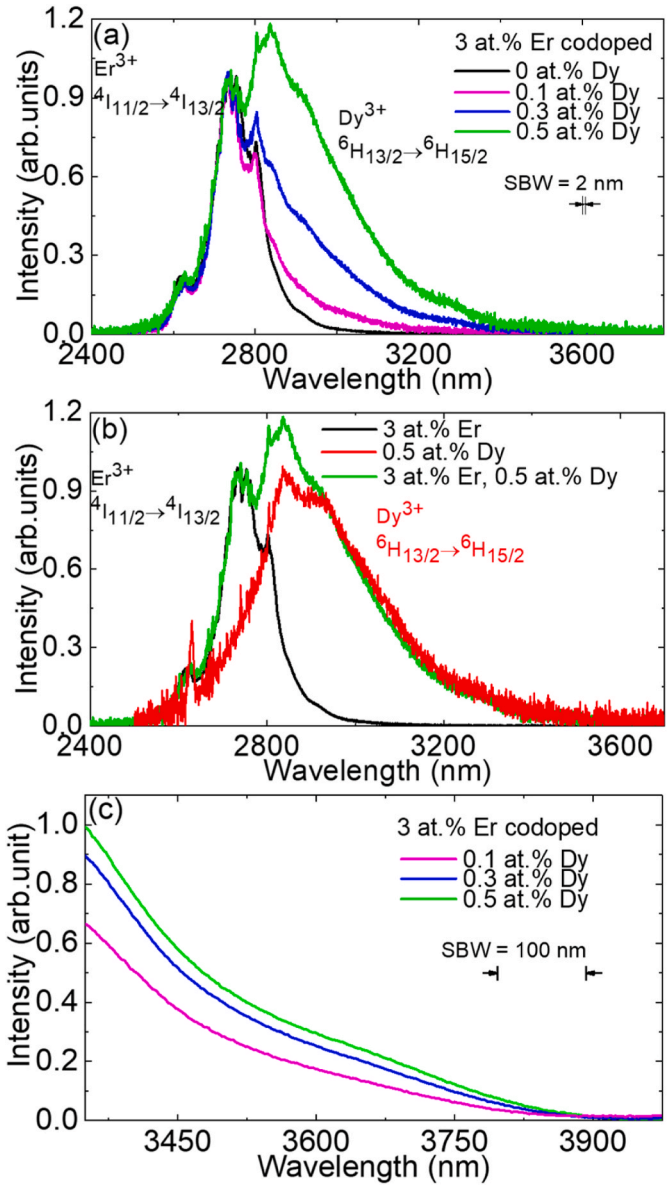

Fig. 6. Spectra of mid-infrared luminescence around 3 μm of (a) 3 at.% Er^{3+}, x at.% Dy^{3+}:CaF_2 crystals with $x = 0$, 0.1, 0.3, and 0.5; (b) deconvolution of the emission spectrum of the 3 at.% Er^{3+}, 0.5 at.% Dy^{3+} codoped crystal using the spectra of the corresponding singly-doped CaF_2 crystals. λ_{exc} = 960 nm (Er), 1320 nm (Dy); (c) Long-wave multiphonon emission sideband of the $^6H_{13/2} \rightarrow {}^6H_{15/2}$ transition of Dy^{3+} ions beyond 3.3 μm.

$_2(Er^{3+}) \rightarrow {}^6H_{11/2}(Dy^{3+})$ process – from 77.4% to 94.0%, when the Dy content changes from $x = 0.1$ at.% to 0.5 at.%.

4.7. 4.4-μm emission of Dy^{3+} ions and non-radiative relaxation

In the present work, we report on the first observation of 4.4-μm emission from Dy^{3+} ions in CaF_2 at room temperature. The SE cross-sections for the $^6H_{11/2} \rightarrow {}^6H_{13/2}$ transition were calculated using the F-L formula based on the measured luminescence spectrum, see Fig. 8. The peak σ_{SE} value reaches 1.36×10^{-20} cm^2 at 4390 nm and the corresponding emission bandwidth (FWHM) is about 100 nm. The luminescence lifetime of this weak emission could not be directly measured at room temperature.

The luminescence lifetime of the $^6H_{11/2}$ manifold of 15 μs was estimated from the radiative lifetime calculated using the Judd-Ofelt theory, and the rate of multiphonon non-radiative relaxation extracted

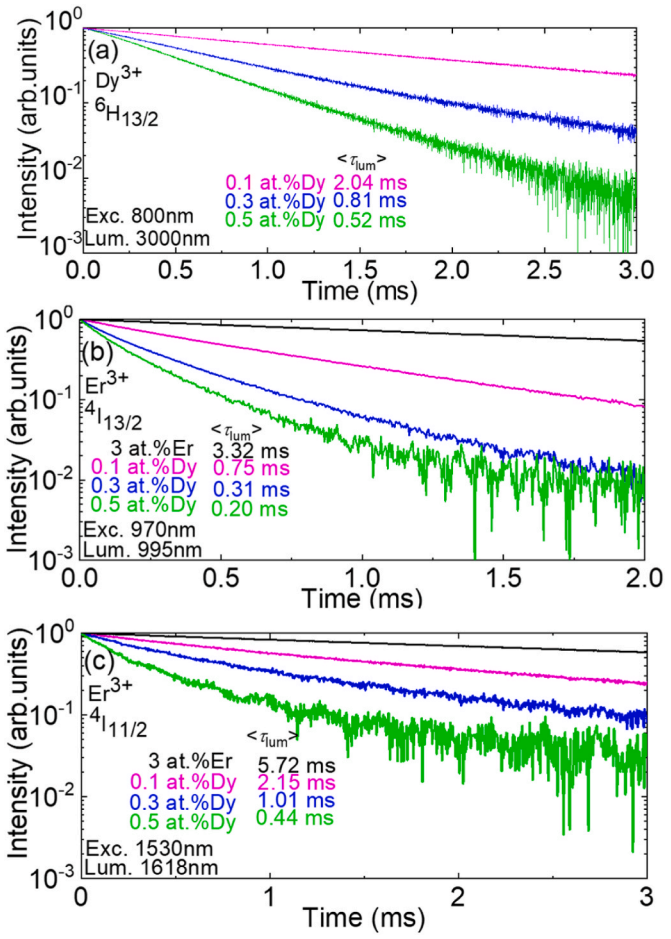

Fig. 7. (a-c) Luminescence decay curves from (a) $^6H_{13/2}$ Dy^{3+}, (b,c) $^4I_{13/2}$ and $^4I_{11/2}$ Er^{3+} manifolds in 3 at.% Er, x at.% Dy:CaF_2 crystals with $x = 0.1$, 0.3, and 0.5, $<\tau_{lum}>$ – mean luminescence lifetime. In (b,c), the data for 3 at.% Er singly-doped CaF_2 are added for comparison.

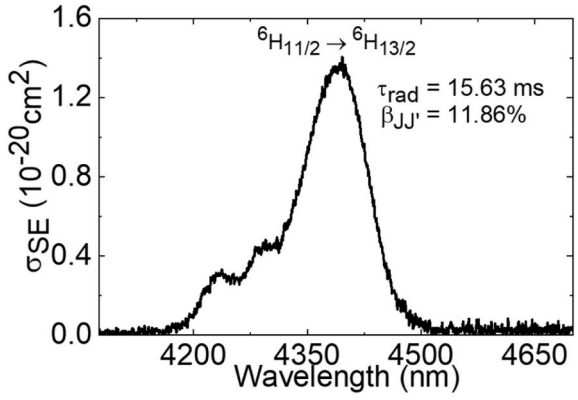

Fig. 8. Stimulated-emission (SE), σ_{SE}, cross-sections for the $^6H_{11/2} \rightarrow {}^6H_{13/2}$ transition of Dy^{3+} ions in CaF_2.

form the exponential bandgap law, $(1/\tau_{lum}) = (1/\tau_{rad}) + W_{NR}$. The rate of multiphonon non-radiative relaxation is given by Ref. [47]:

$$W_{NR} = Ce^{-\ln(\varepsilon)\frac{\Delta E}{\hbar\omega_{ph}}}, \quad (3)$$

where C is a constant corresponding to the rate of NR relaxation in the limit of zero energy-gap ($\Delta E \rightarrow 0$), and ε is the ratio between the probabilities of m-phonon and m–1-phonon relaxation. By fitting the

available experimental data on W_{NR} for various rare-earth ions (Ho^{3+} [24], Er^{3+} [18] and Dy^{3+} – this work) with Eq. (3), we have obtained the following material parameters: $C = 1.3 \pm 0.6 \times 10^9$ s^{-1} and $\varepsilon = 6.3 \pm 0.7$, see Fig. 9(a). Due to the small energy gap between the $^6H_{11/2}$ and $^6H_{13/2}$ states of around 2500 cm^{-1}, the luminescence lifetime of $^6H_{11/2}$ Dy^{3+} manifold at room temperature is strongly affected by the multiphonon-assisted thermal quenching demonstrated by a sharp drop of the lifetime from ms-range for τ_{rad} to μs-range for τ_{lum}. The non-radiative path from the $^6H_{11/2}$ manifold can be suppressed by cooling the Dy^{3+}:CaF_2 crystal to cryogenic temperatures.

Following the approach of Johnson and Guggenheim [14], we compared the rates of spontaneous dipole radiative transitions of rare-earth ions in CaF_2 – which scale with frequency as $\sim\nu^3$ – with the non-radiative relaxation rates, which decrease approximately exponentially, $\sim e^{-\nu}$, as shown in Fig. 9(b). At ~3 μm, the room-temperature non-radiative decay is less than two orders of magnitude higher than the radiative rate, still permitting laser operation despite a reduced luminescence quantum efficiency. At 4.4 μm, this difference increases to nearly four orders of magnitude, necessitating cryogenic cooling to suppress phonon-assisted relaxation.

A potential laser scheme based on the $^6H_{11/2} \rightarrow {}^6H_{13/2}$ transition of Dy^{3+} ions would be self-terminating due to the significantly longer lifetime of the terminal level compared to that of the upper emitting level. This issue may be mitigated in two ways: i) by employing cascade lasing at both 3 μm and 4.4 μm to depopulate the intermediate $^6H_{13/2}$ manifold, or ii) by codoping with Tb^{3+} ions, which facilitate quenching of the $^6H_{13/2}$ lifetime. Notably, a similar approach has been successfully implemented in yellow Dy^{3+} lasers [48,49], where the non-negligible lifetime of the terminal laser level is undesirable.

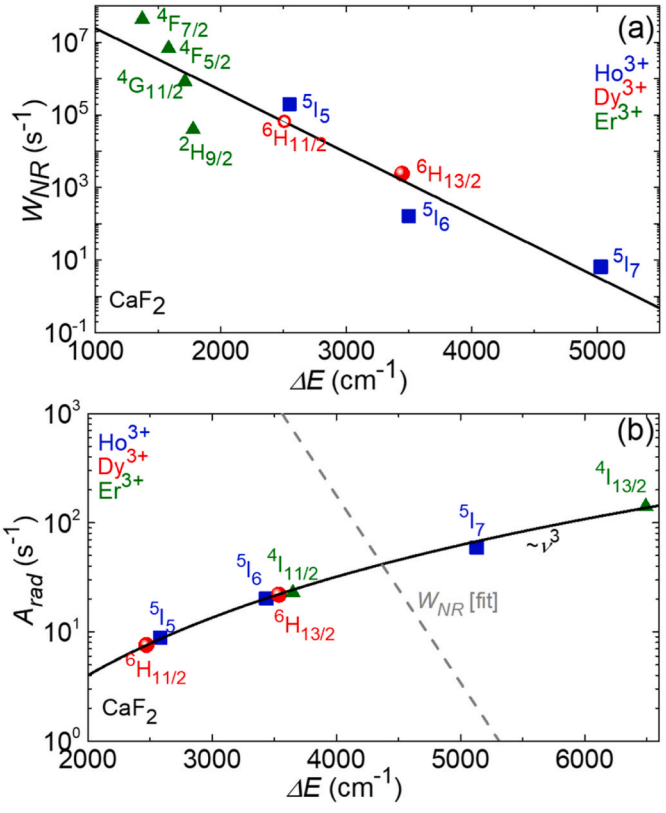

Fig. 9. Probabilities of radiative and non-radiative transitions of rare-earth ions in CaF_2: (a) non-radiative relaxation rate W_{NR} vs. the energy gap to the next lower-lying level ΔE: *symbols* – experimental data derived from the luminescence and radiative lifetimes, *line* – their fit using Eq. (3); (b) probabilities of spontaneous radiative transitions A_{rad} from the emitting manifolds: *symbols* – values obtained using the Judd-Ofelt theory, *curve* – their fit using a ν^3 dependence expected for dipolar transitions.

It is instructive to compare the 4.4 μm emission properties of Dy^{3+} ions in CaF_2 with those of the state-of-the-art mid-infrared-emitting Dy^{3+}-doped crystal KPb_2Cl_5. For this compound, a stimulated-emission cross-section of 0.6×10^{-20} cm^2 at 4.25 μm has been reported, although the polarization state was not specified. The $^6H_{11/2}$ luminescence lifetime τ_{lum} is 6.94 ms, corresponding to a luminescence quantum efficiency of 78% [50]. KPb_2Cl_5 is hygroscopic, and the growth of large-volume crystals with optical quality remains challenging; moreover, the material contains lead.

4.8. Discussion: Dy^{3+} ion in fluorite-type crystals

Within the family of cubic fluorite-type crystals MF_2, the strontium and barium (M = Sr and Ba) counterparts of calcium fluorides are known for yet lower phonon energies. We have directly compared the 3 μm emission properties (spectra and lifetimes) of calcium, strontium, and barium fluorides doped with 0.5 at.% Dy^{3+}. This concentration represents the lower limit at which the activator ions form clusters, thereby avoiding excessive luminescence quenching while enabling a meaningful comparison of multiphonon non-radiative relaxation processes as a function of host phonon energy. At lower doping levels, the contribution from isolated ions becomes significant.

Fig. 10(a) shows the Raman spectra of Dy^{3+}-doped CaF_2, SrF_2 and BaF_2 crystals. At the center of the Brillouin zone $\Gamma(\boldsymbol{k} = 0)$, the factor group theory [51] predicts three optical phonon modes, *i.e.*, a doubly degenerate IR-active mode TO T_{1u}, a triply degenerate Raman-active mode T_{2g}, and an IR-active nondegenerate mode LO T_{1u}. The frequency of the T_{2g} progressively decreases in the M = Ca → Sr → Ba series, measuring 321.5 → 284.0 → 244.9 cm^{-1}, suggesting a decreased non-radiative path.

The spectra of 3-μm luminescence from these crystals, measured under identical excitation and detection conditions, are compared in Fig. 10(b). In the M = Ca → Sr → Ba series, the spectra progressively narrower and become more structured due to the weaker crystal field and decreased diversity of the cluster geometries, while at the same time the luminescence intensity increases. This is in line with a progressive increase of the $^6H_{13/2}$ lifetime, τ_{lum} = 0.63 ms (Dy^{3+}:SrF_2) and 1.13 ms (Dy^{3+}:BaF_2), Fig. 10(c). The corresponding rates of non-radiative relaxation W_{NR} are 1.57×10^3 s^{-1} and 0.86×10^3 s^{-1} and they progressively decrease in the M = Ca → Sr → Ba series.

5. Conclusions

To conclude, calcium fluoride crystals doped with Dy^{3+} ions are promising gain media for broadly tunable lasers operating above 3 μm (on the $^6H_{13/2} \rightarrow {}^6H_{15/2}$ transition), *i.e.*, outside the range of structured water vapor absorption being a severe limiting factor for mid-infrared Erbium lasers, *e.g.*, those employing Er^{3+}:CaF_2 crystals. The Er^{3+},Dy^{3+} codoping scheme resolves the limitation of unconventional pump wavelengths for Dy^{3+}: efficient excitation of 3 μm luminescence is demonstrated by InGaAs diode laser pumping. Codoped crystals exhibit high energy-transfer efficiencies (exceeding 90%, estimated from the shortening of the donor (Er^{3+}) luminescence lifetimes) promoted by the proximity of donor and acceptor (Dy^{3+}) ions forming rare-earth clusters. The Er^{3+},Dy^{3+} codoped CaF_2 crystals also feature increased emission bandwidth due to the spectrally combined luminescence profiles of both active ions. This represents an additional advantage as compared to the alternative Tm^{3+}, Dy^{3+} codoping scheme exploited earlier [52].

In the challenging spectral range of 3 to 4 μm, two emission mechanisms are revealed: i) a phonon-assisted (Stokes) emission related to the $^6H_{13/2} \rightarrow {}^6H_{15/2}$ transition sharing the same upper laser level ($^6H_{15/2}$) lifetime, and ii) a relatively weak emission arising from the $^6H_{11/2} \rightarrow {}^6H_{13/2}$ electronic transition which is in a strong competition with a non-radiative relaxation path. The potential of fluorite-type crystals for emission at 4.4 μm could be further revealed when employing SrF_2 and

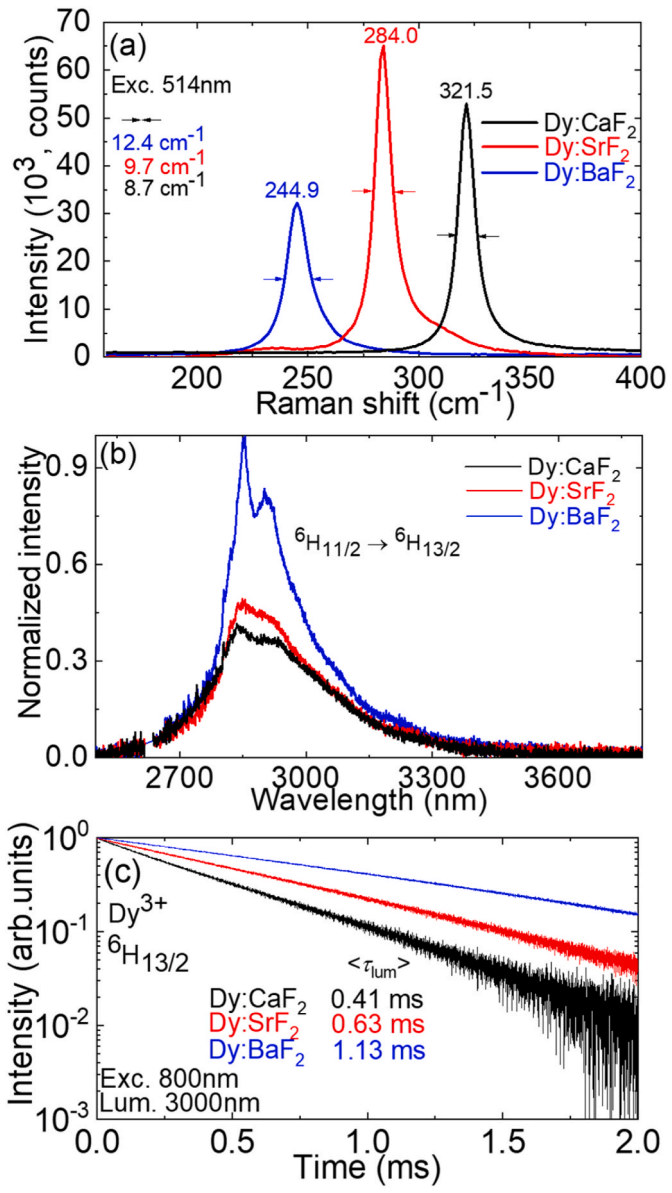

Fig. 10. Comparison of vibronic and mid-infrared emission properties of fluorite-type crystals 0.5 at.% Dy:MF_2 (M = Ca, Sr and Ba): (a) Raman spectra, λ_{exc} = 514 nm, *numbers* – peak frequencies and Raman peak widths (FWHM); (b) luminescence spectra at 3 μm (in scale); (c) Luminescence decay curves from the $^6H_{13/2}$ Dy^{3+} manifold, $<\tau_{lum}>$ – mean luminescence lifetime.

BaF_2 host matrices for Dy^{3+} doping.

Given the high solubility of rare-earth activators in fluorite-type crystals, the study of heavily Dy^{3+}-doped MF_2 systems is of particular interest for identifying the mechanisms responsible for luminescence quenching for the $^6H_{13/2}$ manifold, possibly involving energy migration. The corresponding lifetime may also be influenced by the increasing structural complexity of rare-earth ion clusters at high doping levels.

CRediT authorship contribution statement

Ngoc Quynh Hoa Nguyen: Investigation, Writing – original draft. **Elena Dunina:** Formal analysis, Methodology. **Liudmila Fomicheva:** Formal analysis, Methodology. **Alexey Kornienko:** Data curation, Methodology, Software. **Pavel Popov:** Investigation, Methodology. **Sergei Kuznetsov:** Conceptualization, Investigation, Resources. **Abdelmjid Benayad:** Investigation. **Patrice Camy:** Funding acquisition, Supervision. **Alain Braud:** Funding acquisition, Supervision, Writing – review & editing. **Pavel A. Loiko:** Writing – review & editing, Methodology, Supervision.

Declaration of competing interest

The authors declare that they have no known competing financial interests or personal relationships that could have appeared to influence the work reported in this paper.

Acknowledgments

French Agence Nationale de la Recherche (ANR-25-CE08-4202-02, DUPLEX; ANR-22-CE08-0031, FLAMIR); Région Normandie, France (Contrat de plan État-Région (CPER)).

Data availability

Data will be made available on request.

References

[1] A. Schliesser, N. Picqué, T.W. Hänsch, Mid-infrared frequency combs, Nat. Photonics 6 (2012) 440–449, https://doi.org/10.1038/nphoton.2012.142.
[2] F.K. Tittel, D. Richter, A. Fried, Mid-infrared laser applications in spectroscopy, Top. Appl. Phys. 89 (2003) 458–529, https://doi.org/10.1007/3-540-36491-9_11.
[3] B.M. Walsh, H.R. Lee, N.P. Barnes, Mid infrared lasers for remote sensing applications, J. Lumin. 169 (2016) 400–405, https://doi.org/10.1016/j.jlumin.2015.03.004.
[4] T.M. Taczak, D.K. Killinger, Development of a tunable, narrow-linewidth, CW 2.066-μm Ho:YLF laser for remote sensing of atmospheric CO_2 and H_2O, Appl. Opt. 37 (1998) 8460–8476, https://doi.org/10.1364/AO.37.008460.
[5] J. Ma, Z. Qin, G. Xie, L. Qian, D. Tang, Review of mid-infrared mode-locked laser sources in the 2.0 μm–3.5 μm spectral region, Appl. Phys. Rev. 6 (2019) 021317, https://doi.org/10.1063/1.5037274.
[6] Y.O. Aydin, V. Fortin, R. Vallée, M. Bernier, Towards power scaling of 2.8 μm fiber lasers, Opt. Lett. 43 (2018) 4542–4545, https://doi.org/10.1364/OL.43.004542.
[7] J. Li, D.D. Hudson, S.D. Jackson, High-power diode-pumped fiber laser operating at 3 μm, Opt. Lett. 36 (2011) 3642–3644, https://doi.org/10.1364/OL.36.003642.
[8] M.R. Majewski, R.I. Woodward, S.D. Jackson, Dysprosium mid-infrared lasers: current status and future prospects, Laser Photonics Rev. 14 (2020) 1900195, https://doi.org/10.1002/lpor.201900195.
[9] N.P. Barnes, E.A. Roger, Room temperature Dy:YLF laser operation at 4.34 μm, IEEE J. Quant. Electron. 27 (2002) 277–282, https://doi.org/10.1109/3.78231.
[10] M.C. Nostrand, R.H. Page, S.A. Payne, W.F. Krupke, P.G. Schunemann, Room-temperature laser action at 4.3–4.4 μm in $CaGa_2S_4$:Dy^{3+}, Opt. Lett. 24 (1999) 1215, https://doi.org/10.1364/OL.24.001215.
[11] R.I. Woodward, M.R. Majewski, G. Bharathan, D.D. Hudson, A. Fuerbach, S. D. Jackson, Watt-level dysprosium fiber laser at 3.15 μm with 73% slope efficiency, Opt. Lett. 43 (2018) 1471–1474, https://doi.org/10.1364/OL.43.001471.
[12] M.R. Majewski, R.I. Woodward, S.D. Jackson, Dysprosium-doped ZBLAN fiber laser tunable from 2.8 μm to 3.4 μm, pumped at 1.7 μm, Opt. Lett. 43 (2018) 971–974, https://doi.org/10.1364/OL.43.000971.
[13] J. Jung, K. Lee, J. Kim, I. Kim, J.H. Lee, An experimental and theoretical study on Dy^{3+}-doped ZBLAN fiber laser core-pumped at 1.1 μm, Laser Phys. 34 (2024) 045103, https://doi.org/10.1088/1555-6611/ad2dd1.
[14] L.F. Johnson, H.J. Guggenheim, Laser emission at 3 μm from Dy^{3+} in BaY_2F_8, Appl. Phys. Lett. 23 (1973) 96–98, https://doi.org/10.1063/1.1654822.
[15] J. Wang, X. Zhu, R.A. Norwood, N. Peyghambarian, Widely wavelength tunable Dy^{3+}/Er^{3+} co-doped ZBLAN fiber lasers, Opt. Express 29 (2021) 38646–38653, https://doi.org/10.1364/OE.443808.
[16] H. Jelínková, M.E. Doroshenko, M. Jelínek, J. Šulc, V.V. Osiko, V.V. Badikov, D. V. Badikov, Dysprosium-doped $PbGa_2S_4$ laser generating at 4.3 μm directly pumped by 1.7 μm laser diode, Opt. Lett. 38 (2013) 3040–3043, https://doi.org/10.1364/OL.38.003040.
[17] P. Schlosser, L. Isaenko, A. Tarasova, V. Savitski, Diode-pumped Dy:KPb_2Cl_5 laser in the middle-infrared spectral region, Opt. Lett. 47 (2022) 1553–1556, https://doi.org/10.1364/OL.454156.
[18] S. Normani, P. Loiko, L. Basyrova, A. Benayad, A. Braud, E. Dunina, L. Fomicheva, A. Kornienko, A. Hideur, P. Camy, Mid-infrared emission properties of erbium-doped fluorite-type crystals, Opt. Mater. Express 13 (2023) 1836–1851, https://doi.org/10.1364/OME.482402.
[19] P. Camy, J.L. Doualan, A. Benayad, M.V. Edlinger, V. Ménard, R. Moncorgé, Comparative spectroscopic and laser properties of Yb^{3+}-doped CaF_2, SrF_2 and BaF_2 single crystals, Appl. Phys. B 89 (2007) 539–542, https://doi.org/10.1007/s00340-007-2829-x.
[20] F. Druon, S. Ricaud, D.N. Papadopoulos, A. Pellegrina, P. Camy, J.L. Doualan, R. Moncorgé, A. Courjaud, E. Mottay, P. Georges, On Yb:CaF_2 and Yb:SrF_2: review of spectroscopic and thermal properties and their impact on femtosecond and high power laser performance, Opt. Mater. Express 1 (2011) 489–502, https://doi.org/10.1364/OME.1.000489.

[21] L. Basyrova, P. Loiko, J.L. Doualan, A. Benayad, A. Braud, B. Viana, P. Camy, Thermal lensing, heat loading and power scaling of mid-infrared Er:CaF_2 lasers, Opt. Express 30 (2022) 8092–8103, https://doi.org/10.1364/OE.449129.

[22] E.A. Sulyanova, V.N. Molchanov, I.A. Verin, S.N. Sulyanov, B.P. Sobolev, Nanostructured crystals of the fluorite phases $Sr_{1-x}R_xF_{2+x}$ (R—Rare-earth elements) and their ordering: II. Crystal structure of the ordered $Sr_4Lu_3F_{17}$ phase, Crystallogr. Rep. 54 (2009) 516–525, https://doi.org/10.1134/S1063774509030249.

[23] V. Petit, P. Camy, J.-L. Doualan, X. Portier, R. Moncorgé, Spectroscopy of Yb^{3+}:CaF_2: from isolated centers to clusters, Phys. Rev. B 78 (2008) 085131, https://doi.org/10.1103/PhysRevB.78.085131, 1-12.

[24] N.Q.H. Nguyen, P. Loiko, A. Benayad, E. Dunina, L. Fomicheva, A. Kornienko, P. Camy, A. Braud, Prospects of low-phonon energy Ho:MF_2 (M = Ca, Sr, Ba) crystals for 2-3 μm lasers, Opt. Express 33 (2025) 24303–24320, https://doi.org/10.1364/OE.558443.

[25] Y. Wang, J. Liu, X. Feng, Z. Zhang, Y. Wang, Z. Zhang, F. Ma, J. Liu, L. Su, ~2.9 μm continuous-wavelength laser operation of fiber-pumped Ho,Pr:CaF_2 single crystals, Opt. Mater. 135 (2023) 113329, https://doi.org/10.1016/j.optmat.2022.113329, 2023.

[26] S.V. Kuznetsov, P.P. Fedorov, Morphological stability of solid-liquid interface during melt crystallization of $M_{1-x}R_xF_{2+x}$ solid solutions, Inorg. Mater. 44 (2008) 1434–1458, https://doi.org/10.1134/S0020168508130037.

[27] P.A. Popov, A.A. Sidorov, E.A. Kul'chenkov, A.M. Anishchenko, I.C. Avetissov, N. I. Sorokin, P.P. Fedorov, Thermal conductivity and expansion of PbF_2 single crystals, Ionics 23 (2017) 233–239, https://doi.org/10.1007/s11581-016-1802-2.

[28] P.A. Popov, K.V. Dukelsky, I.A. Mironov, A.N. Smirnov, P.L. Smolyansky, P. P. Fedorov, V.V. Osiko, T.T. Basiev, Thermal conductivity of CaF_2 optical ceramics, Dokl. Phys. 52 (2007) 7–9, https://doi.org/10.1134/S1028335807010028.

[29] D.S. Moore, J.C. Wright, Laser spectroscopy of defect chemistry in CaF_2: Er^{3+}, J. Chem. Phys. 74 (1981) 1626–1636, https://doi.org/10.1063/1.441303.

[30] S.A. Kazanskii, A.I. Ryskin, A.E. Nikiforov, A.Y. Zaharov, M.Y. Ougrumov, G. S. Shakurov, EPR spectra and crystal field of hexamer rare-earth clusters in fluorites, Phys. Rev. B Condens. Matter 72 (2005) 014127, https://doi.org/10.1103/PhysRevB.72.014127.

[31] P.P. Fedorov, S.V. Kuznetsov, V.V. Osiko, Elaboration of nanofluorides and ceramics for optical and laser applications. Photonic and Electronic Properties of Fluoride Materials, Elsevier, 2016, pp. 7–31, https://doi.org/10.1016/B978-0-12-801639-8.00002-7.

[32] W.T. Carnall, P.R. Fields, K. Rajnak, Electronic energy levels in the trivalent lanthanide aquo ions. I. Pr^{3+}, Nd^{3+}, Pm^{3+}, Sm^{3+}, Dy^{3+}, Ho^{3+}, Er^{3+}, and Tm^{3+}, J. Chem. Phys. 49 (1968) 4424–4442, https://doi.org/10.1063/1.1669893.

[33] M.Z. Amin, M.R. Majewski, R.I. Woodward, A. Fuerbach, S. Jackson, Novel near-infrared pump wavelengths for dysprosium fiber lasers, J. Lightwave Technol. 38 (2020) 5801–5808. https://opg.optica.org/jlt/abstract.cfm?URI=jlt-38-20-5801.

[34] Y.H. Tsang, A.E. El-Taher, T.A. King, S.D. Jackson, Efficient 2.96 μm dysprosium-doped fluoride fibre laser pumped with a Nd:YAG laser operating at 1.3 μm, Opt. Express 14 (2006) 678–685, https://doi.org/10.1364/OPEX.14.000678.

[35] R. Švejkar, A.G. Papashvili, J. Šulc, M. Němec, H. Jelínková, M.E. Doroshenko, S. H. Batygov, V.V. Osiko, 2.4 μm diode-pumped Dy^{2+}:CaF_2 laser, Laser Phys. Lett. 15 (2017) 015803, https://doi.org/10.1088/1612-202X/aa806d.

[36] K.A. Gschneidner, J.C.G. Bunzli, V.K. Pecharsky, Handbook on the Physics and Chemistry of Rare Earths, vol. 34, 2004. V.1. Metals. Part 3.

[37] S.E. Hatch, W.F. Parsons, R.J. Weagley, Hot-pressed polycrystalline CaF_2:Dy^{2+} laser, Appl. Phys. Lett. 5 (1964) 153–154, https://doi.org/10.1063/1.1754094.

[38] E.M. Zolotov, A.M. Prokhorov, G.P. Shipulo, Luminescence and generation in CaF_2:Dy^{2+} crystals excited with a ruby laser, Zh. Eksp. Teor. Fiz. 22 (1966) 498–500 [In Russian].

[39] S.K. Isaev, L.S. Kornienko, E.G. Lariontsev, Emission kinetics of a hemispherical-cavity CaF_2:Dy^{2+} laser, Sov. J. Quant. Electron. 3 (1974) 388–391, https://doi.org/10.1070/QE1974v003n05ABEH005531.

[40] A.A. Kornienko, A.A. Kaminskii, E.B. Dunina, Dependence of the line strength of f–f transitions on the manifold energy. II. Analysis of Pr^{3+} in $KPrP_4O_{12}$, Phys. Status Solidi B 157 (1) (1990) 267–273, https://doi.org/10.1002/pssb.2221570127.

[41] Z. Pan, P. Loiko, S. Slimi, H. Yuan, X. Dai, H. Cai, Y. Wang, Y. Zhao, R.M. Solé, M. Aguiló, F. Díaz, P. Camy, E. Dunina, A. Kornienko, L. Fomicheva, U. Griebner, V. Petrov, X. Mateos, Tm,Ho:Ca(Gd,Lu)AlO_4 crystals: crystal growth, structure refinement and Judd–Ofelt analysis, J. Lumin. 246 (2022) 118828, https://doi.org/10.1016/j.jlumin.2022.118828.

[42] H.H. Li, Refractive index of alkaline earth halides and its wavelength and temperature derivatives, J. Phys. Chem. Ref. Data 9 (1980) 161–290, https://doi.org/10.1063/1.555616.

[43] X. Gao, G. Fang, Y. Wang, Z. Zhu, Z. You, J. Li, C. Tu, Visible and mid-infrared spectral performances of Dy^{3+}:CaF_2 and Dy^{3+}/Y^{3+}:CaF_2 crystals, J. Alloys Compd. 856 (2021) 158083, https://doi.org/10.1016/j.jallcom.2020.158083.

[44] Z.D. Fleischman, E.E. Brown, J. Rosen, M. Dubinskii, Spectroscopic investigation of dysprosium doped BaF_2 single crystals pertaining to the 3 μm mid-IR laser potential, Opt. Mater. Express 11 (2021) 3496–3506, https://doi.org/10.1364/OME.438716.

[45] B. Aull, H. Jenssen, Vibronic interactions in Nd:YAG resulting in nonreciprocity of absorption and stimulated emission cross sections, IEEE J. Quant. Electron. 18 (1682) 925–930. https://doi.org/10.1109/JQE.1982.1071611.

[46] H. Nara, M. Schlesinger, Analysis of the optical spectra of Dy^{3+} doped calcium fluoride, J. Phys. C Solid State Phys. 5 (1972) 606, https://doi.org/10.1088/0022-3719/5/5/012.

[47] M.P. Miller, J.C. Wright, Multiphonon and energy transfer relaxation in charge compensated crystals, J. Chem. Phys. 71 (1979) 324–338, https://doi.org/10.1063/1.438074.

[48] G. Bolognesi, D. Parisi, D. Calonico, G.A. Costanzo, F. Levi, P.W. Metz, C. Kränkel, G. Huber, M. Tonelli, Yellow laser performance of Dy^{3+} in co-doped Dy,Tb:$LiLuF_4$, Opt. Lett. 39 (2014) 6628–6631, https://doi.org/10.1364/OL.39.006628.

[49] Q. Xu, L. Sun, B. Zhang, J. Li, J. Gao, C. Nie, X. Shi, S. Sun, B. Teng, Y. Zhang, D. Zhong, Crystal growth and spectroscopic performances of Dy^{3+}:YPO_4 and Dy^{3+}/Tb^{3+}:YPO_4 crystal as potential yellow laser gain media, J. Alloys Compd. 996 (2024) 174855, https://doi.org/10.1016/j.jallcom.2024.174855.

[50] M.C. Nostrand, R.H. Page, S.A. Payne, W.F. Krupke, P.G. Schunemann, L.I. Isaenko, Room temperature $CaGa_2S_4$:Dy^{3+} laser action at 2.43 and 4.31 μm and KPb_2Cl_5:Dy^{3+} laser action at 2.43 μm, in: Advanced Solid State Lasers, Optica Publishing Group, 1999, https://doi.org/10.1364/ASSL.1999.WD4 paper WD4.

[51] J.P. Russell, The Raman spectrum of calcium fluoride, Proc. Phys. Soc. 85 (1965) 194–199, https://doi.org/10.1088/0370-1328/85/1/129.

[52] G. Brasse, R. Soulard, J.L. Doualan, A. Braud, A. Benayad, P. Camy, Tm^{3+} codoping for mid-infrared laser applications of Dy^{3+}-doped CaF_2 crystals, J. Lumin. 232 (2021) 117852, https://doi.org/10.1016/j.jlumin.2020.117852.